All Pseudocapacitive MXene-RuO$_2$ Asymmetric Supercapacitors

Qiu Jiang, Narendra Kurra, Mohamed Alhabeb, Yury Gogotsi, and Husam N. Alshareef*

2D transition metal carbides and nitrides, known as MXenes, are an emerging class of 2D materials with a wide spectrum of potential applications, in particular in electrochemical energy storage. The hydrophilicity of MXenes combined with their metallic conductivity and surface redox reactions is the key for high-rate pseudocapacitive energy storage in MXene electrodes. However, symmetric MXene supercapacitors have a limited voltage window of around 0.6 V due to possible oxidation at high anodic potentials. In this study, the fact that titanium carbide MXene (Ti$_3$C$_2$T$_x$) can operate at negative potentials in acidic electrolyte is exploited, to design an all-pseudocapacitive asymmetric device by combining it with a ruthenium oxide (RuO$_2$) positive electrode. This asymmetric device operates at a voltage window of 1.5 V, which is about two times wider than the operating voltage window of symmetric MXene supercapacitors, and is the widest voltage window reported to date for MXene-based supercapacitors. The complementary working potential windows of MXene and RuO$_2$, along with proton-induced pseudocapacitance, significantly enhance the device performance. As a result, the asymmetric devices can deliver an energy density of 37 µW h cm^{-2} at a power density of 40 mW cm^{-2}, with 86% capacitance retention after 20 000 charge–discharge cycles. These results show that pseudocapacitive negative MXene electrodes can potentially replace carbon-based materials in asymmetric electrochemical capacitors, leading to an increased energy density.

Electrochemical energy storage devices have recently gained increasing attention, thanks to high demand from electronics, smart textiles, electrical vehicles, and renewable energy generators.[1,2] The energy and power density of any energy storage device is governed by the fundamental charge storage mechanism and the associated kinetics at the electrode/electrolyte interface. Batteries, for example, utilize reversible redox reactions involving mobile metal ion insertion into the bulk of the electrode material. As a result, they exhibit high energy density,

Q. Jiang, Dr. N. Kurra, Prof. H. N. Alshareef
Materials Science and Engineering
King Abdullah University of Science and Technology (KAUST)
Thuwal 23955–6900, Saudi Arabia
E-mail: husam.alshareef@kaust.edu.sa
Dr. N. Kurra, M. Alhabeb, Prof. Y. Gogotsi
Department of Materials Science and Engineering
A.J. Drexel Nanomaterials Institute
Drexel University
Philadelphia, PA 19104, USA

but suffer from low power density due to slow diffusion-controlled processes.[3,4] On the other hand, electrochemical double-layer capacitors (EDLCs), also known as supercapacitors, exhibit high power densities, fast charge–discharge (CD) rates, and long cycle lives, which allow them to complement batteries for high power applications.[5–7] EDLCs store charge through electrostatic adsorption of electrolyte ions onto high surface area carbonaceous materials without charge transfer, so their capacity is limited by the surface area accessible to the electrolyte ions. In contrast, pseudocapacitive materials, such as metal oxides or conducting polymers, store charge through reversible surface redox reactions at high charge–discharge rates, which means that they can have energy density comparable to batteries while exhibiting power density similar to electric double-layer capacitors (EDLCs).[8] However, low electronic conductivity and poor cycling stability limit the power density and lifetime of conventional pseudocapacitive materials.

Recently, a large family of 2D transition metal carbides and nitrides, collectively referred to as MXenes, have shown great promise as high-rate electrodes for pseudocapacitive energy storage due to their highly reversible surface redox reactions and metallic electrical conductivity.[9,10] Usually, MXenes have been synthesized from ternary layered ceramic materials known as MAX phases, which can be represented by the general formula $M_{n+1}AX_n$, where M is a transition metal (e.g., Ti, Nb, Mo, V, Cr, and Ta), A is an element from groups 13 or 14 in the periodic table (e.g., Al, Si, Ga, and In), and X is carbon (C) and/or nitrogen (N), with $n = 1$, 2, or 3.[10] Generally, synthesis of MXenes involves selective etching of the A group element from the MAX phase using hydrofluoric acid (HF). The resulting MXenes can be represented by the general formula $M_{n+1}X_nT_x$, where T_x denotes the surface termination groups such as −F, −O, and −OH, which are responsible for the hydrophilicity of MXenes.[11,12]

Titanium carbide (Ti$_3$C$_2$T$_x$), which is the first reported and the most studied MXene, can be synthesized by selective removal of aluminum from Ti$_3$AlC$_2$ using HF-forming or HF-containing etchants.[13] Since the discovery of MXenes in 2011 by Drexel scientists,[11] Ti$_3$C$_2$T$_x$ MXene in particular has gained significant attention for many applications including supercapacitors[14,15] and metal-ion batteries and capacitors.[16–18] The

ADVANCED
SCIENCE NEWS
www.advancedsciencenews.com

ADVANCED
ENERGY
MATERIALS
www.advenergymat.de

high metallic conductivity (up to 8000 S cm^{-1}),[13] packing density (4 g cm^{-3}), and redox chemistry at the metal oxide/hydroxide surfaces with tunable functionality are the most striking features of Ti$_3$C$_2$T$_x$ MXene. These properties led to high-rate performance, high specific volumetric capacitances in the range of 1000–1500 F cm^{-3},[9] and excellent cycling stability in acidic electrolyte.[14,15] However, symmetric supercapacitor devices based on Ti$_3$C$_2$T$_x$ have shown limited operating voltage windows (≈0.6 V) because Ti$_3$C$_2$T$_x$ is prone to oxidation at higher anodic potentials (for example, anodic oxidation was observed in a symmetric two-electrode configuration at ≥0.6 V).[19,20] Recently, it has been shown that Ti$_3$C$_2$T$_x$ MXene electrodes are electrochemically stable in acidic electrolyte at higher cathodic potentials when metal current collectors are replaced by hydrogen overpotential materials, such as glassy carbon or graphite foil.[9] This resulted in a wider negative potential window operation of Ti$_3$C$_2$T$_x$ MXene electrodes (up to −1.1 V vs Hg/Hg$_2$SO$_4$),[9] unlike the previous studies with a limited potential window.[14,15]

In general, carbon-based materials have been employed as negative electrodes in combination with positive pseudocapacitive electrodes for designing various asymmetric supercapacitors (redox//EDLC type).[21] However, the capacitance of such asymmetric device is limited by the electrode with the lowest capacitive–carbon ($1/C_T = 1/C_+ + 1/C_-$, where C_T is total capacitance, C_+ and C_- are capacitances of positive and negative electrodes, respectively).[22] Since MXene is a pseudocapacitive material that operates in the negative potential window,[9] combining it with another positive pseudocapacitive material can widen the voltage window of operation. This could result in devices with a higher energy density compared to asymmetric devices using carbon as the negative electrode (energy density, $E = 1/2CV^2$).[23]

To demonstrate our concept, we chose ruthenium oxide (RuO$_2$) as the positive electrode among various pseudocapacitive materials because of its high conductivity, large proton-induced pseudocapacitance, and high overpotential for oxygen evolution in acidic media.[24,25] Hydrous RuO$_2$ was first demonstrated as a pseudocapacitive material in acidic electrolyte in 1971,[26] and it has been attracting attention ever since due to its high capacitance.[8] The redox pseudocapacitance of RuO$_2$ is largely attributed to the transport of protons from the electrolyte into the nanocrystal boundaries.[27] Further, the optimal pseudocapacitance of RuO$_2$.xH$_2$O can be achieved when the electronic and protonic transport are balanced by changing the content of structural water within the materials lattice, which leads to a maximum theoretical capacitance of 1450 F g^{-1} over a 1 V potential window.[28] In addition, there have been some studies focusing on design of asymmetric supercapacitors based on RuO$_2$ with carbon-based materials,[29–31] but never with MXenes.

Here, we demonstrate the fabrication of a fabric-based asymmetric pseudocapacitor by combining positive RuO$_2$ with negative Ti$_3$C$_2$T$_x$ electrodes in acidic electrolyte. Carbon fabric (CF) is inexpensive and offers good electrical conductivity and a 3D texture which allows for a large loading of electrode materials in a given footprint area. Therefore, carbon fabric was chosen in our study as the substrate for direct deposition of both MXene and RuO$_2$ without the need for any surface pretreatment or use of binders or conductive additives. The all-pseudocapacitive asymmetric devices employing 2D metal carbides and metal oxides could open up a new direction in development of MXene-based energy storage devices.

The schematic representation shown in **Figure 1**a illustrates the synthesis process of Ti$_3$C$_2$T$_x$ MXene. Ti$_3$C$_2$T$_x$ MXene was synthesized using the minimal intensive layer delamination (MILD) method in which manual shaking of the resulting Ti$_3$C$_2$T$_x$ powder suspension in water is enough to achieve delamination, leading to stable aqueous colloidal solution of MXene (synthesis details are provided in the Experimental Section). The morphologies of Ti$_3$AlC$_2$ precursor and Ti$_3$C$_2$T$_x$ MXene nanosheets are shown in Figure S1, Supporting Information. It has been demonstrated that stable colloidal solutions of Ti$_3$C$_2$T$_x$ can be processed by various means, including spray and spin coating on a wide choice of substrates, such as glass,[32] plastic, and Si wafers.[19,33] However, these substrates are insulating and often require a pretreatment to enhance the hydrophilicity of their surfaces, which is needed to improve the adhesion of Ti$_3$C$_2$T$_x$. We chose porous textured conductive CF as substrate for loading the electrode materials. The 3D texture of CFs (Panel 1, Figure 1b) eliminates the need for using binders and facilitates the adhesion of electroactive materials, resulting in an increase in the mass loading of active material in a given footprint area. Additionally, CF is chemically inert and has been demonstrated as a compatible substrate for depositing a wide choice of materials, in comparison to metal current collectors. These attributes of CF are ideal for the proposed asymmetric devices and hence it was chosen as a conductive substrate to load Ti$_3$C$_2$T$_x$ by drop casting (Panel 2, Figure 1b). As shown in Panel 3 in Figure 1b, hydrous RuO$_2$ was grown hydrothermally on the CF, where ruthenium chloride (RuCl$_3$) was used as the precursor with different mass loadings (see Experimental Section for details). The all-pseudocapacitive asymmetric capacitor was then assembled by stacking the RuO$_2$/CF positive electrode and Ti$_3$C$_2$T$_x$/CF negative electrode in acidic electrolyte (Panel 4, Figure 1b).

The structural characteristics of RuO$_2$/CF and Ti$_3$C$_2$T$_x$/CF were investigated by X-ray diffraction. As shown in **Figure 2**a, RuO$_2$/CF shows only a weak and broad peak at 55°, while the CF has strong and broad peaks at $2\theta = 26.2°$ and 43.5°, which apparently interfere with the diffraction peaks of RuO$_2$/CF. To overcome this issue, RuO$_2$ powder was removed from the CF and separately used for X-ray diffraction (XRD) analysis (Figure S2, Supporting information). RuO$_2$ powder showed broad diffraction peaks at 28.4°, 35.8°, and 55.2° (PDF#73–1469), which are in agreement with previous literature reports.[27] The broad diffraction peaks indicate the nanocrystalline nature of the hydrous RuO$_2$.[34] Ti$_3$C$_2$T$_x$/CF electrode shows strong (002) peak centered at 2θ of 6.9° (FWHM = 0.5°), which corresponds to a d-spacing of 1.3 nm (see Figure 2a), confirming the coating of MXene on carbon fiber. Raman spectra of Ti$_3$C$_2$T$_x$/CF and RuO$_2$/CF are shown in Figure 2b. The typical signatures of Ti$_3$C$_2$T$_x$ at 208, 280, 627, and 727 cm^{-1} are seen with the D and G peaks of CF as well.[35] For RuO$_2$, three main peaks are observed at 514, 630, and 695 cm^{-1}, which can be assigned to E_g, A_{1g}, and B_{2g} modes of RuO$_2$, respectively.[36] As shown in Figure 2c,e, both the RuO$_2$ and Ti$_3$C$_2$T$_x$ were uniformly deposited over the entire exposed surface of the carbon fabric. RuO$_2$ particles were seen

ADVANCED
SCIENCE NEWS
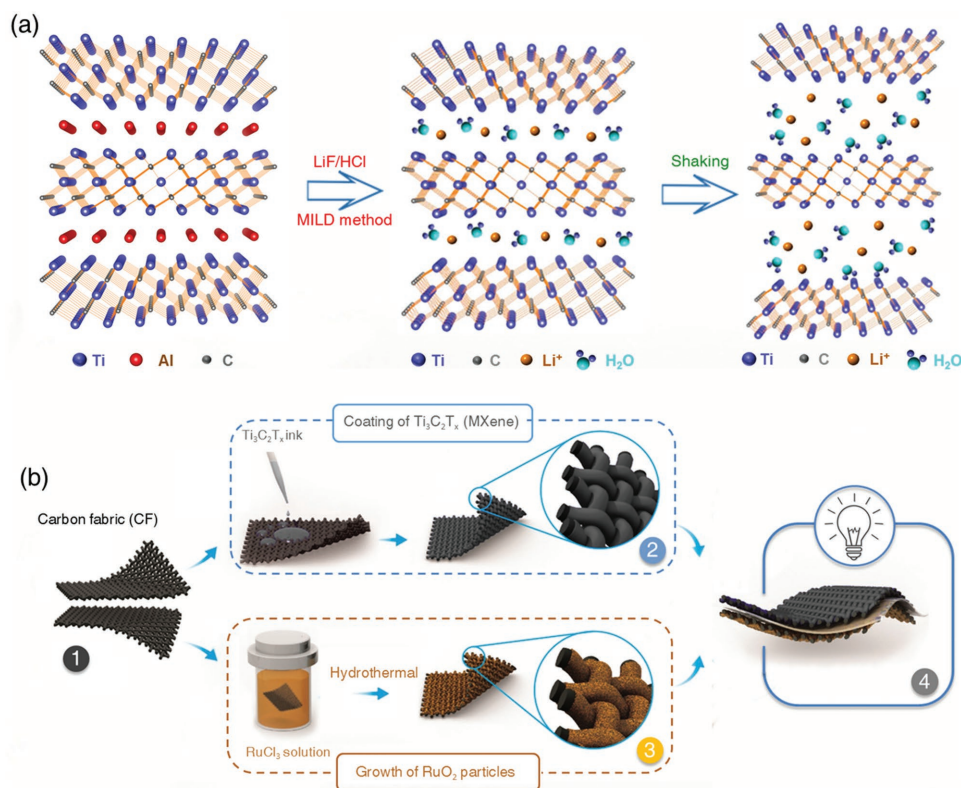www.advancedsciencenews.com

ADVANCED
ENERGY
MATERIALS
www.advenergymat.de

Figure 1. Fabrication of an all-pseudocapacitive asymmetric supercapacitor a) synthesis scheme of $Ti_3C_2T_x$ MXene; surface functional groups are not shown for the sake of simplicity. b) Schematic representation illustrating the fabrication process of asymmetric supercapacitor. Panel 1 represents 3D textured CF. Panels 2 and 3 represent the coating of $Ti_3C_2T_x$ MXene on CF by drop casting and growth of amorphous RuO_2 over CF by hydrothermal synthesis, respectively. Panel 4 represents the RuO_2//$Ti_3C_2T_x$ asymmetric pseudocapacitor.

to be densely packed on the individual carbon fibers, as shown in the scanning electron microscope (SEM) microscopy image of Figure 2d. Similarly, $Ti_3C_2T_x$ MXene flakes were uniformly coated over the carbon fiber, which is again evident from the SEM microscopy image shown in Figure 2f. Digital photographs of the CF, $Ti_3C_2T_x$/CF, and RuO_2/CF are also shown in Figure S3, Supporting information where visual appearance of the different color gradients indicates uniform coatings of both $Ti_3C_2T_x$ and RuO_2 over the CF.

The electrochemical performance of $Ti_3C_2T_x$/CF and RuO_2/CF electrodes was evaluated in deaerated 1 M sulfuric acid (H_2SO_4) in a three-electrode configuration. Cyclic voltammograms (CVs) of $Ti_3C_2T_x$ (mass loading of 0.8 mg cm^{-2}) are shown in **Figure 3**a. A pair of broad redox peaks can be observed in the potential window of −0.7 to 0.2 V (vs Ag/AgCl) at different scan rates. The redox reactions of $Ti_3C_2T_x$ can be explained by reversible intercalation/deintercalation of protons, which is responsible for changes in oxidation state of Ti.[37] A small shift in anodic and cathodic peak positions were observed with increasing scan rate (anodic: −0.4 to −0.3 V, cathodic: −0.49 to −0.52 V), indicating the reversible nature of redox reactions at the surface. However, the shift observed in the anodic peak position was slightly larger than the cathodic peak shift. This might be due to the ion desorption process (hydronium debonding from surface functional groups), which is the controlling kinetic step for the ion-exchange process. To understand the kinetic effect of the

anodic scan, sweep analysis was performed using CVs at different scan rates. The total charge stored can be separated into two main components: (i) pseudocapacitive component due to fast Faradaic charge-transfer process with surface atoms, and non-Faradaic contribution from the double layer adsorption of ions. (ii) Diffusion-controlled Faradaic intercalation processes. The measured current i from CV curves obeys power law relationship with the sweep rate, v[38]

$$i = ab^v \tag{1}$$

where "a" and "b" are adjustable parameters. For diffusion-controlled processes, the current response is proportional to the square root of the scan rate ($b = 0.5$); on the other hand, for a capacitive process, the current response is proportional to the scan rate ($b = 1$). As shown in Figure 3b, b-values obtained at different potentials were in the range of 0.85–1, indicating that the current response is mainly capacitive in the potential window of −0.7 to 0.2 V (vs Ag/AgCl). This is in good agreement with previous reports on the pseudocapacitive nature of $Ti_3C_2T_x$ electrodes.[9,14] To further distinguish and quantify the capacitive contribution to the overall current response, we assume current response at a fixed potential as being the combination of two separate mechanisms, surface capacitive effects, and diffusion-controlled insertion processes
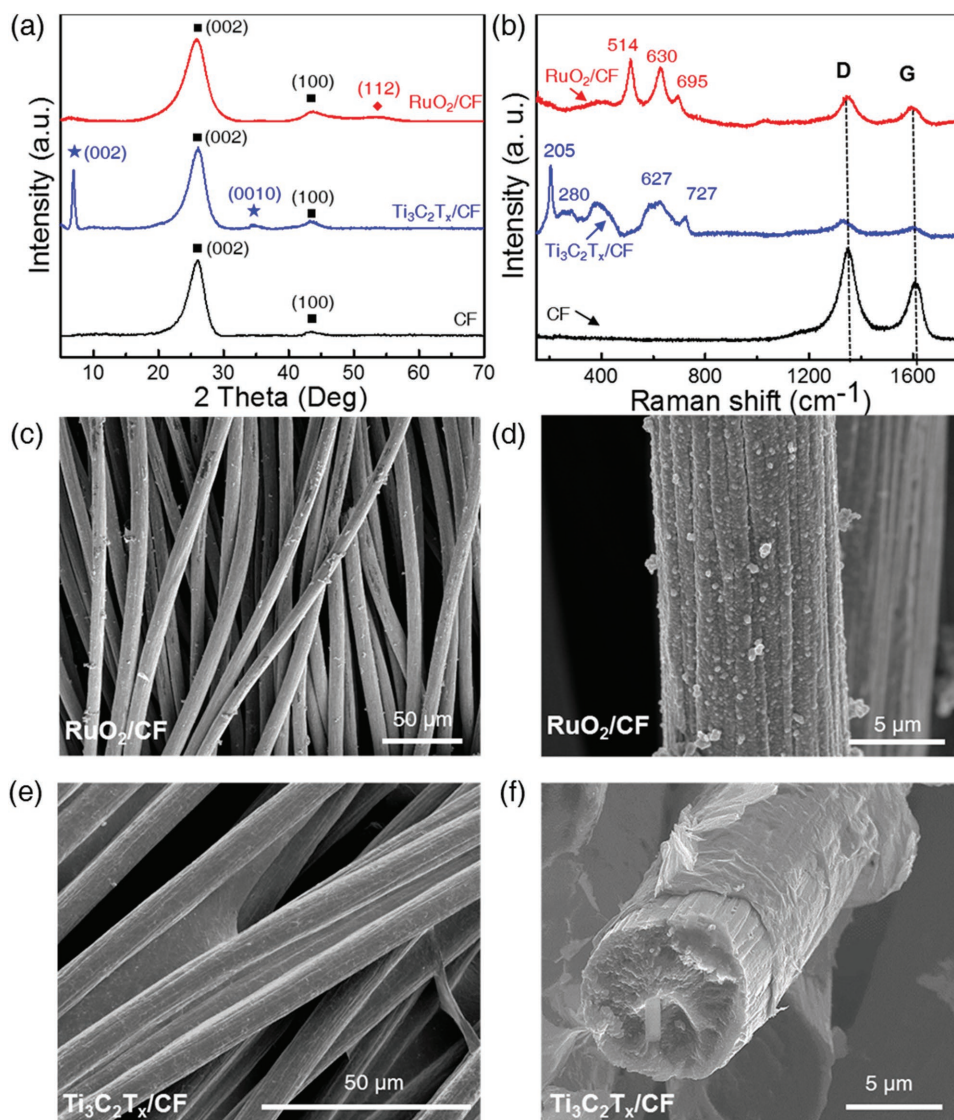
Figure 2. a) XRD patterns of $Ti_3C_2T_x/CF$, RuO_2/CF, and CF. Squares represent (002) and (100) diffraction peaks of graphitic carbon, ◆ is for (112) peak of RuO_2 and ★ is for (001) peaks of $Ti_3C_2T_x$ b) Raman spectra of $Ti_3C_2T_x/CF$, RuO_2/CF, and CF. Low c) and high d) magnification field emission scanning electron microscopy images of RuO_2/CF. e) Low magnification SEM image showing uniform coating of $Ti_3C_2T_x$ on carbon fibers. f) Wrapped $Ti_3C_2T_x$ flakes over an individual fiber of the carbon fabric.

$$i(V) = k_1 \upsilon + k_2 \upsilon^{1/2} \qquad (2)$$

where υ is the scan rate (mV s^{-1}), $k_1\upsilon$ and $k_2\upsilon^{1/2}$ represent the currents from surface capacitance contribution and the diffusion-controlled Faradaic processes, respectively. Equation (2) can also be rearranged to

$$\frac{i(V)}{\upsilon^{\frac{1}{2}}} = k_1 \upsilon^{\frac{1}{2}} + k_2 \qquad (3)$$

So, k_1 and k_2 can be derived from the linear plot of $i(V)/\upsilon^{1/2}$ versus $\upsilon^{1/2}$ with different scan rates. Surface capacitive and diffusion-controlled processes were separated using Equation (3). As shown in Figure 3a, the shaded region

corresponds to capacitive contribution which is estimated to be around 75% at a scan rate of 50 mV s^{-1}.

Galvanostatic charge–discharge curves of the $Ti_3C_2T_x/CF$ electrodes were measured at current densities from 5 to 30 A g^{-1}, as shown in Figure 3c. The observed deviation from the triangular-shaped charge–discharge curves typical for EDLC electrodes is due to predominant surface redox reactions of $Ti_3C_2T_x$, which is in agreement with the CV analysis. Additionally, the charge–discharge profiles were quite symmetric, with Coulombic efficiencies close to 100%, indicating the reversible nature of surface redox reactions of $Ti_3C_2T_x$ electrodes. As shown in Figure 3d, the $Ti_3C_2T_x/CF$ electrode at low mass loading of 0.8 mg cm^{-2} exhibits a gravimetric capacitance (per weight of active material) of 401 F g^{-1} (corresponding charge of 360 C g^{-1}) at a scan rate of 10 mV s^{-1}; which decreases to 350 F g^{-1} at
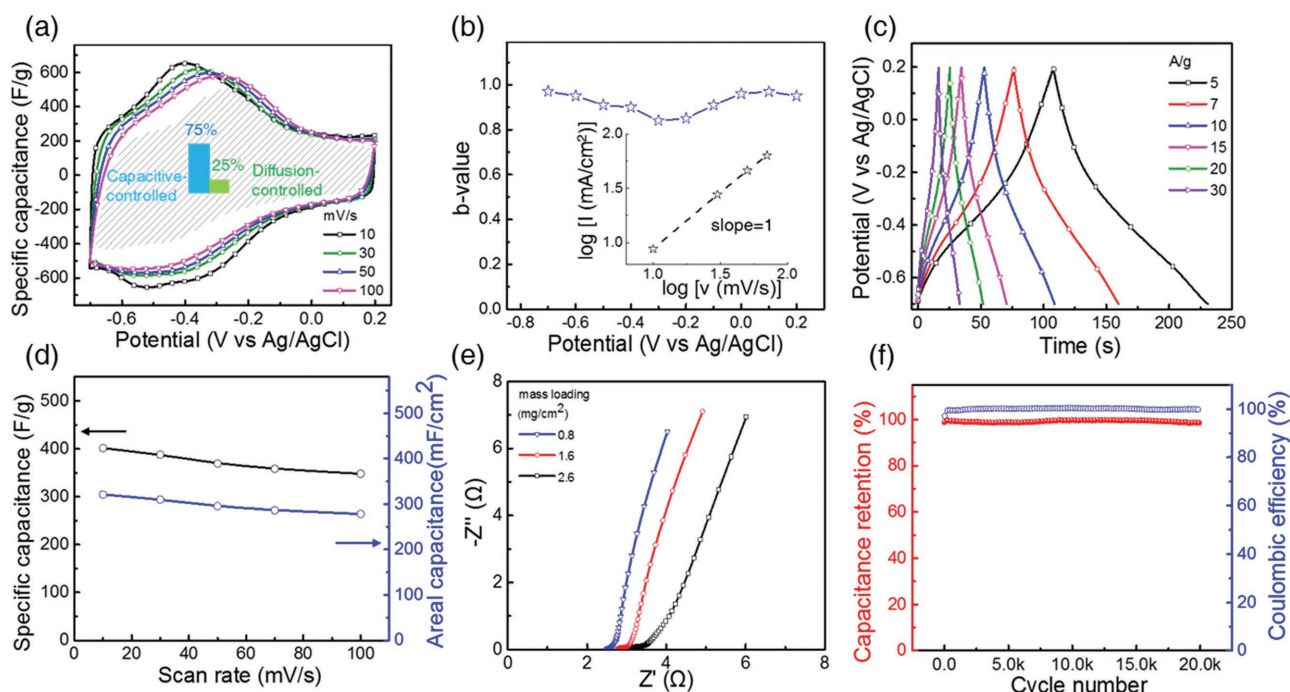
ADVANCED
SCIENCE NEWS
www.advancedsciencenews.com

ADVANCED
ENERGY
MATERIALS
www.advenergymat.de

Figure 3. Electrochemical performance of $Ti_3C_2T_x$/CF in 1 M H_2SO_4 in three-electrode configuration. a) CV curves at different scan rates, where shaded area represents the contribution of capacitive current at a scan rate of 50 mV s^{-1}. b) Variation of *b*-values as a function of potential for anodic scan. Inset shows power-law dependence of peak current density at scan rates from 10 to 100 mV s^{-1}. c) Galvanostatic charge–discharge profiles of $Ti_3C_2T_x$/CF at different current densities. d) Gravimetric and areal capacitances of $Ti_3C_2T_x$/CF at different scan rates. e) Nyquist plots of $Ti_3C_2T_x$/CF with different mass loadings. f) Cycling stability and Coulombic efficiency of $Ti_3C_2T_x$ MXene over 20k cycles at a current density of 20 A g^{-1}.

a scan rate of 100 mV s^{-1}, that corresponds to a capacitance retention of 87%. The $Ti_3C_2T_x$/CF electrode shows very competitive gravimetric capacitance values (refer to Table S1, Supporting Information), probably due to good Ohmic coupling between the deposited $Ti_3C_2T_x$ and CF, as well as short transport/diffusion path lengths for protons and electrons. Variation in capacitance with respect to mass loading was also studied, and the corresponding data are shown in Figure S5, Supporting information. As expected, the specific areal capacitance (per geometric area of electrode) increased from 320 to 416 mF cm^{-2}, when the mass loading was increased from 0.8 to 2.6 mg cm^{-2}. However, gravimetric capacitance values decreased from 401 to 200 F g^{-1} with increasing mass loading, a fact that can be attributed to underutilization of the electrochemically active surface area.[39] It is shown that thinner electrodes often with lower mass loadings show higher gravimetric capacitance.[4,9] From the Nyquist plot shown in Figure 3e, equivalent series resistance (ESR) values were found to be 2.5–3 Ω for different mass loadings of $Ti_3C_2T_x$ with a small semicircle in the high frequency region. This ESR value comes apparently from CF, as $Ti_3C_2T_x$ has a very low resistance.[9] The long-term cycling test was conducted in 1 M H_2SO_4 at a high current density of 20 A g^{-1} over 20 000 cycles (Figure 3f), where a capacitance retention of 98% was observed.

As shown in **Figure 4**a, CVs of RuO$_2$/CF clearly show a pair of very broad redox peaks in the chosen potential window (0–0.9 V vs Ag/AgCl), which is indicative of pseudocapacitive behavior of RuO$_2$. Using Equation (3), we have determined that the primary contribution to the capacitance of RuO$_2$ electrodes

(95%) comes from the capacitive-controlled redox processes rather than diffusion-limited processes (Figure S6, Supporting information). The capacitive-type fast kinetics in both RuO$_2$/CF and $Ti_3C_2T_x$/CF electrodes indicate the fast surface redox reactions, which are responsible for the high rate performance of our devices.

The galvanostatic charge/discharge curves in Figure 4b show nearly symmetric triangular-shaped curves with clear redox signatures at around 0.3 V. The Ohmic drop is small even at a high current density of 20 A g^{-1}, implying good conductivity of the RuO$_2$/CF electrodes. The RuO$_2$ electrode delivers a specific capacitance of 388 F g^{-1} (at a scan rate of 10 mV s^{-1}) and retains up to 355 F g^{-1} at 100 mV s^{-1}, which corresponds to rate retention of 91% (Figure 4c). Long-term cycling test was conducted in 1 M H_2SO_4 at a high current density of 20 A g^{-1} over 20 000 cycles (Figure 4d), showing that 88% of the initial capacitance was retained while maintaining 100% Coulombic efficiency. The collective resistive contributions from current collectors, electrode materials, and electrolyte resistance were found to be 6 Ω as obtained from the intercept in the high frequency region of Nyquist plot (see inset of Figure 4d).

To optimize the performance of the asymmetric device prior to assembly, the mass loading of the two electrodes was balanced using Equation S1 (Supporting Information). The corresponding charge balance chart is shown in Table S2, Supporting Information. **Figure 5**a displays the potential windows of the RuO$_2$ (0–0.9 V) and $Ti_3C_2T_x$ (−0.7 to 0.2 V) electrodes at the same scan rate of 50 mV s^{-1}, showing that a similar amount of charge is being stored on each electrode. The asymmetric
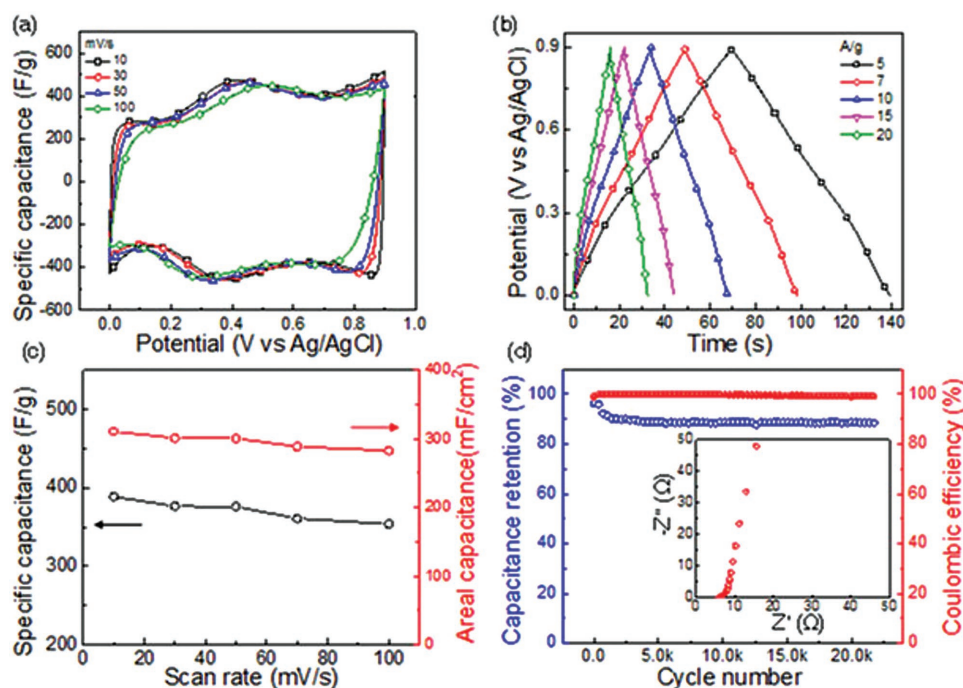
Figure 4. Electrochemical performance of RuO$_2$/CF in 1 M H$_2$SO$_4$ in three-electrode configuration: a) CV curves at different scan rates. b) Galvanostatic charge–discharge profiles of RuO$_2$/CF electrode at different current densities. c) Variation of gravimetric and areal capacitances with scan rates. d) Cycling stability and Coulombic efficiency of RuO$_2$/CF over 20k cycles at a current density of 20 A g^{-1}; inset shows Nyquist plot of an RuO$_2$/CF electrode.

device (with total active material mass loading of 1.55 mg cm^{-2}) was assembled by sealing the positive and negative electrodes in a plastic bag, with a porous polymer membrane (Celgard 3501) as the separator (see inset of Figure 5b). The maximum operating voltage for the proposed asymmetric supercapacitor based on the three-electrode measurements can reach 1.6 V. However, there is always a trade-off between the maximum operating voltage and the cycle life of a supercapacitor.[40] To maximize the cycle life, we chose 1.5 V as the maximum operating voltage of the asymmetric device. Figure 5b shows CVs of the asymmetric device, where a pair of pronounced redox peaks is observed at 0.6 and 0.7 V; these peaks indicate that the dominant charge storage mechanism in the asymmetric device is Faradaic in nature. As shown in Figure 5b, the asymmetric device can be operated at a high scan rate of 1000 mV s^{-1}, which is due to the good electrical conductivity of RuO$_2$ and Ti$_3$C$_2$T$_x$ electrodes. Charge–discharge profiles in Figure 5c show a curvature at similar voltages as the CVs, which can be attributed to the pseudocapacitive nature of the electrode materials. As shown in Figure 5d, at a scan rate of 50 mV s^{-1}, the device delivers a capacitance of 93 F g^{-1} and maintains a capacitance of 78 F g^{-1} when the scan rate is increased to 1000 mV s^{-1}. This high-rate performance can be attributed not only to capacity matching, but also to kinetic balance and fast redox kinetics of both electrodes. Furthermore, the high-rate performance is confirmed by the small characteristic relaxation time constant τ_0 (the minimum time needed to discharge all the energy with efficiency greater than 50%) of 740 ms (Figure 5e). The asymmetric device exhibits good cycling stability with a capacitance retention of 86% and a Coulombic efficiency of 100% over 20 000 cycles, as shown in Figure 5f.

For comparison, we have also fabricated a Ti$_3$C$_2$T$_x$ symmetric device with the same mass loading on both electrodes. As shown in Figure S8 (Supporting Information), the symmetric MXene device has a smaller voltage window of 0.9 V (compared to 1.5 V of asymmetric device), which is limited by the oxidation of the positive Ti$_3$C$_2$T$_x$ MXene electrode at high anodic potentials. The electrochemical performance of our asymmetric device can be compared with other recently published state-of-the-art asymmetric devices. Based on the weight of active material, our devices show an energy density of 29 W h kg^{-1} at a power density of 3.8 kW kg^{-1}, and an energy density of 24 W h kg^{-1} at a power density of 26 kW kg^{-1} (Figure S9a, Supporting Information). Moreover, it is worth noting that the asymmetric device performance was measured with discharge times of 30–1.5 s (corresponding CV scan rates are from 50 to 1000 mV s^{-1}). When compared with early conventional electrochemical capacitors (with energy densities below 10 W h kg^{-1}) and state-of-the-art pseudocapacitive symmetric/asymmetric devices[30,41,42] (these reports consider only weight of active electrode materials for the calculation), our devices show superior energy and power densities. It should be noted that most of these reports used carbon-based materials/composites as the negative electrode materials in designing asymmetric supercapacitors. These results clearly show that MXene electrodes can be employed to replace carbon-based materials in high-energy asymmetric supercapacitors. Using the maximum current, our device can be charged in less than 1 s, which is comparable to charging times of carbon-based EDLCs. We have also calculated the device performance based on its entire mass (including current collector, separator, electrolyte, and active materials) and find that the device delivers an energy density of 1.8 W h kg^{-1}
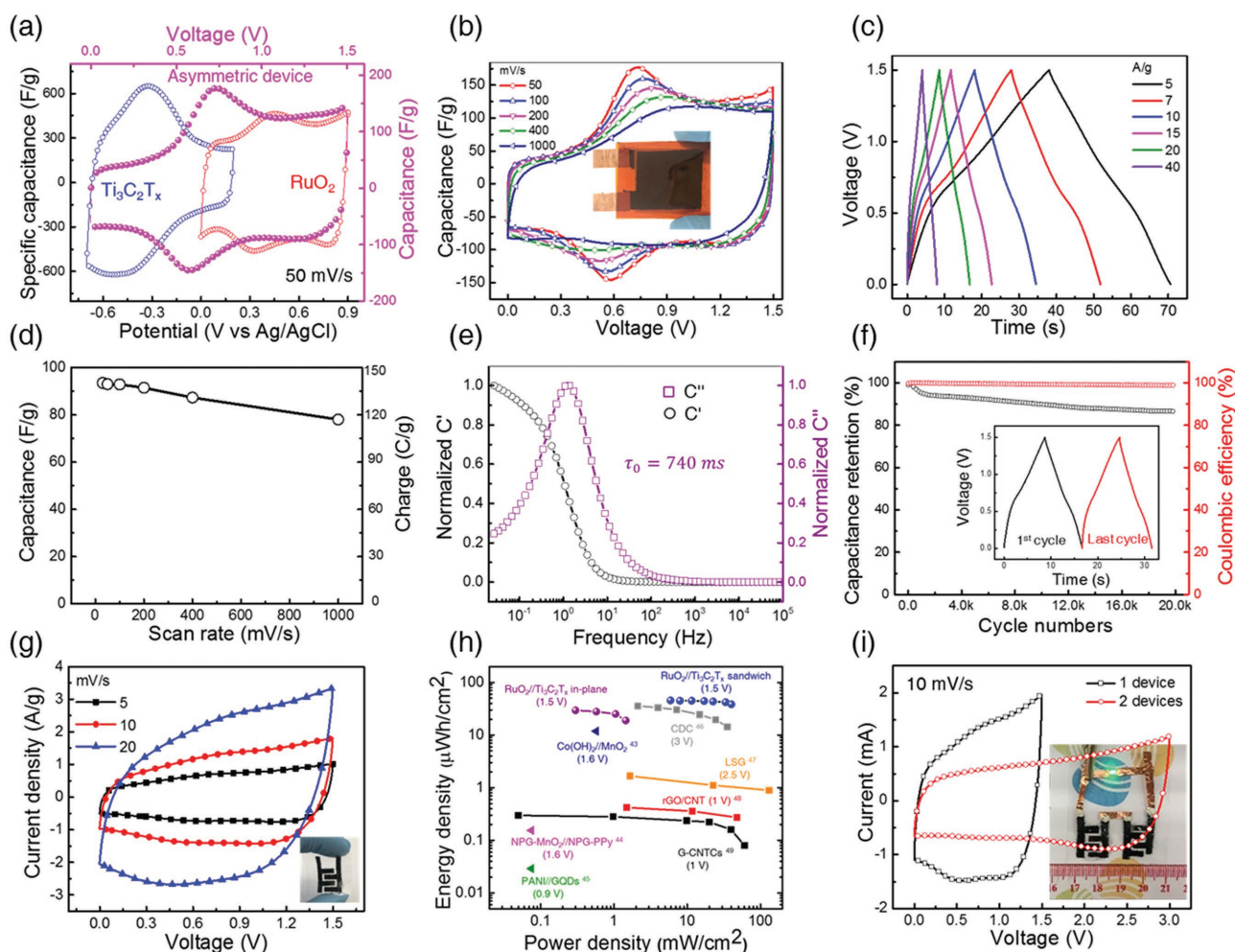
Figure 5. Electrochemical performance of $RuO_2//Ti_3C_2T_x$ full-cell device: a) CVs of RuO_2/CF, $Ti_3C_2T_x/CF$, and the asymmetric device at a scan rate of 50 mV s^{-1}. b) CVs of $RuO_2//Ti_3C_2T_x$ asymmetric sandwich device at different scan rates, inset shows the digital photograph of the asymmetric device. c) Galvanostatic charge–discharge curves at different current densities, d) variation of cell capacitance and charge of the asymmetric device at different scan rates. e) Normalized real (C′) and imaginary (C″) parts of capacitance versus frequency of the device. f) Cycling stability and Coulombic efficiency of the asymmetric device over 20 000 cycles in 1 M H_2SO_4 electrolyte at a current density of 20 A g^{-1}, inset show the typical charge–discharge profiles for the first and last charge–discharge cycles. g) CVs of asymmetric in-plane device; inset shows optical image for the in-plane solid-state device attached to polypropylene substrate. h) Ragone plot displaying areal energy and power densities of $RuO_2//Ti_3C_2T_x$ device in comparison to the other state-of-the-art microsupercapacitors, square represents carbon-based microsupercapacitors, triangle represents pseudocapacitive asymmetric microsupercapacitors. i) Cyclic voltammograms of the $RuO_2//Ti_3C_2T_x$ tandem in-plane devices at scan rate of 10 mV s^{-1}. Inset shows that two devices connected in series can power up a green LED during the discharge state.

at a power density of 0.3 kW kg^{-1}, and an energy density of 1.1 W h kg^{-1} at a power density of 2.7 kW kg^{-1} (Figure S9b, Supporting Information). Although we have shown the concept of expanding operation voltage window of MXene based supercapacitors, future studies should be focused on improving cell capacitance, energy density, and ESR values of MXene-based devices.

Since liquid electrolytes may have leakage problems in microscale and wearable applications, in-plane asymmetric solid-state devices were fabricated with gel electrolyte. Since CF is thick (0.4 mm) with a rough surface texture, conventional microfabrication and patterning techniques cannot be used. Instead, we used laser engraving process to form comb-type CF electrodes followed by manual alignment of these fingers to fabricate the in-plane device. Figure 5g shows CVs of

the in-plane solid-state device measured at different scan rates in the operating voltage window of 1.5 V. The in-plane device delivers an areal capacitance of 60 mF cm^{-2} at a scan rate of 5 mV s^{-1} and maintains a capacitance of 50 mF cm^{-2} when scan rate is increased to 20 mV s^{-1}. To compare with other devices, we have also plotted the Ragone plot comparing areal energy and power densities with different in-plane supercapacitors, as shown in Figure 5h. Our in-plane asymmetric device delivers an energy density of 19 μW h cm^{-2} at a power density of 1.5 mW cm^{-2}, showing better performance than other in-plane pseudocapacitive asymmetric microsupercapacitors. However, the power density is lower than EDLC carbon based in-plane microsupercapacitors, which we attribute to the relatively large spacing between the electrode fingers used in our process (1500 μm).[43–45] On the other hand, the asymmetric

sandwich structure fabricated using $RuO_2//Ti_3C_2T_x$ device delivers a power density of 40 mW cm^{-2} at an energy density of 37 μW h cm^{-2}, which is comparable to the state-of-the-art carbon-based symmetric microsupercapacitors, but at higher energy density.[46–49] Since the in-plane devices were fabricated by laser cutting, power density is limited by wide interspaces, as well as the usage of gel electrolyte. To demonstrate that our device can be used in real applications, tandem in-plane devices were fabricated by connecting two asymmetric devices in series to deliver 3 V (Figure 5i). This device could power a 3 V light-emitting diode (LED) as shown in the inset of Figure 5i.

We have demonstrated the fabrication of all-pseudocapacitive asymmetric supercapacitors by combining $Ti_3C_2T_x$ MXene and hydrous RuO_2 electrodes on carbon fabric. This is the widest reported voltage window for electrochemical capacitors having an MXene electrode in aqueous electrolyte. (Voltage window comparison of other $Ti_3C_2T_x$ MXene devices reported in the literature is shown in Table S3, Supporting Information). The complementary potential windows of these two electrodes resulted in an asymmetric device ($RuO_2//Ti_3C_2T_x$) with a voltage window of 1.5 V and measured energy densities of 45 and 37 μW h cm^{-2} at power densities of 6 and 40 mW cm^{-2}, respectively. Our study shows that all-pseudocapacitive MXene-RuO_2 devices are promising for use with aqueous electrolytes, allowing for an expanded voltage window and increased energy density.

Experimental Section

Synthesis of Delaminated $Ti_3C_2T_x$ MXene: All chemicals were used as received without further purification. Layered ternary carbide Ti_3AlC_2 (MAX phase) powder was purchased from Carbon-Ukraine ltd. (particle size < 40 μm). $Ti_3C_2T_x$ MXene was synthesized following MILD method by selective etching of aluminum from Ti_3AlC_2 using in situ HF-forming etchant as we reported in detail elsewhere.[13] The etching solution was prepared by adding 1 g lithium fluoride (LiF, Alfa Aesar, 98+%) to 20 mL 9 M hydrochloric acid (Fisher, technical grade, 35–38%), followed by stirring for 5 min. 1.5 g of Ti_3AlC_2 powder was slowly added to the MILD etchant at room temperature and stirred for 24 h. The acidic suspension was washed with deionized (DI) water until pH ≥ 6 via centrifugation at 3500 rpm (5 min per cycle) and decanting the supernatant after each cycle. Around pH ≥ 6, stable dark green supernatant of $Ti_3C_2T_x$ was observed and then collected after 30 min centrifugation at 3500 rpm. The concentration of $Ti_3C_2T_x$ dispersion was measured by filtering specific amounts of colloidal solution through a polypropylene filter paper (0.064 μm pore size, 3501 Coated PP, Celgard LLC, Charlotte, NC), followed by drying under vacuum at 70 °C overnight.

Preparation of MXene Electrodes: Prior to the drop casting of $Ti_3C_2T_x$, a piece of carbon fabric (ELAT, Fuel Cell Store USA, with mass density of CF and electrolyte of around 13 mg cm^{-2}) was cleaned by acetone, ethanol, and DI water followed by blowing N_2 gas. Then MXene dispersion was drop cast on the carbon fabric followed by drying in oven at 50 °C. This process was repeated several times to obtain the desired mass loading. $Ti_3C_2T_x$ coated on carbon fabric was free from binders or additional conductive additives.

Preparation of RuO_2 Electrodes: RuO_2 electrodes were obtained by immersing a piece of carbon fabric (1 × 3 cm) in a 40 mL of solution containing 0.6 g of $RuCl_3$•xH_2O in a 50 mL autoclave. After heating at 180 °C for 20 h, the as-synthesized sample was washed with DI water and then annealed at 150 °C for 1 h.

Fabrication of Asymmetric Devices: $Ti_3C_2T_x$/CF and RuO_2/CF electrodes were used directly as negative and positive electrodes, respectively, in 1 M H_2SO_4. The asymmetric devices were assembled in pouch cells by sealing them in plastic bags. 1 M H_2SO_4 was used as the electrolyte and

a porous polymer membrane (Celgard 3501) was used as the separator. Polydimethylsiloxane was drop casted and cured under 80 °C as a sealant to avoid creeping of electrolyte from the bottom of the CF to the top to ensure the proper contact between the CF and the alligator clips of the electrochemical instrument.

Electrochemical Measurements: The electrochemical tests (CV, galvanostatic charge–discharge, and electrochemical cycling stability) were conducted at room temperature using a VMP3 electrochemical workstation (BioLogic, France). Electrochemical impedance spectroscopy measurements were performed using a ModuLab (Solartron Analytical) electrochemical workstation in the frequency range from 100 kHz to 0.01 Hz at open circuit potential by applying a small sinusoidal potential signal with an amplitude of 10 mV. For three-electrode measurements, $Ti_3C_2T_x$/CF and RuO_2/CF electrodes were employed as the working electrodes with platinum and Ag/AgCl as the counter and reference electrodes, respectively.

Preparation of Gel Electrolyte: The polyvinyl alcohol (PVA)/H_2SO_4 gel electrolyte was prepared as follows: 1 g of H_2SO_4 was added into 10 mL of deionized water, followed by the addition of 1 g of PVA powder. The whole mixture was heated to 85 °C while stirring until the solution became clear. The solution was used after cooling down to room temperature.

In-Plane Asymmetric Supercapacitor Fabrication: A CO_2 Universal Laser Cutter System (model: Professional laser system PLS6.75, wavelength of 10.6 μm) was used to fabricate interdigitated carbon fabric fingers by direct laser engraving.[50] The averaged focused beam size was around 120 μm. Laser power was set to 60 W at a scan rate of 0.2 cm s^{-1} and pulse per inch was always set to 1000. After cutting, the individual comb fingers were used to deposit $Ti_3C_2T_x$ and RuO_2 separately. After the deposition of materials, they were manually aligned on a plastic substrate followed by pouring the gel electrolyte onto the electrodes and then curing in air for 10 min.

Calculations: Gravimetric-specific capacitance C_m (F g^{-1}) of electrode materials was calculated from the CV curves by integrating the discharge portion using the following equation

$$C_m = \frac{1}{Vm\nu} \int i\,dV \tag{4}$$

where i is the current (mA), V is the potential window (V), ν is the scan rate (mV s^{-1}), and m is the mass of the active material (mg).

Two-electrode configuration (device measurements)

Gravimetric capacitance, $\quad C_g = \frac{1}{VM\nu} \int i\,dV \tag{5}$

where i is the current (mA), V is the voltage window of the device (V), ν is the potential scan rate (mV s^{-1}), and M is the mass of the active electrode materials in both electrodes (mg)

Areal capacitance, $\quad C_A = \frac{M}{A} C_g \tag{6}$

where A is the geometrical footprint area of the device. For sandwich devices, since two electrodes are stacked face to face, we used the area of one electrode. In case of in-plane devices, the total area of both electrodes was considered

Gravimetric energy density, $\quad E_g = \frac{1}{M} \int iV\,dt \tag{7}$

Gravimetric power density, $\quad P_g = \frac{E_g}{\Delta t} \tag{8}$

where Δt is the discharge time

Areal energy density, $\quad E_A = \frac{M}{A} E_g \tag{9}$

Areal power density, $\quad P_A = \frac{M}{A} P_g \tag{10}$

Impedance spectra

The real (C′) and imaginary (C″) parts of capacitances were calculated using the following equations

$$C' = -Z''/\left(2\pi f\, A|Z|^2\right) \tag{11}$$

$$C'' = Z'/\left(2\pi f\, A|Z|^2\right) \tag{12}$$

where $|Z|$ is the absolute value of impedance (Ω), Z' and Z'' are the real and imaginary components of impedance; f is the frequency (Hz).

Material Characterization: XRD patterns were collected by a Bruker diffractometer (D8 Advance) with Cu Kα radiation, $\lambda = 1.5406$ Å. The morphology and microstructure of the samples were characterized by an SEM (Nova Nano 630, FEI). Raman measurements were carried out on the samples using a micro-Raman spectrometer (LabRAM ARAMIS, Horiba-Jobin Yvon) with notch filters cutting at 100 cm^{-1} using a Cobalt laser (633 nm, 5 mW at source). For $Ti_3C_2T_x$/CF, D2 filter (corresponding to 10% of laser power) was used to prevent laser-induced oxidation during the measurements.

Supporting Information

Supporting Information is available from the Wiley Online Library or from the author.

Conflict of Interest

The authors declare no conflict of interest.

[1] P. Simon, Y. Gogotsi, *Nat. Mater.* **2008**, *7*, 845.
[2] M. Winter, R. J. Brodd, *Chem. Rev.* **2004**, *104*, 4245.
[3] P. Simon, Y. Gogotsi, B. Dunn, *Science* **2014**, *343*, 1210.
[4] Y. Gogotsi, P. Simon, *Science* **2011**, *334*, 917.
[5] Y. Gogotsi, *Nature* **2014**, *509*, 568.
[6] J. R. Miller, P. Simon, *Science* **2008**, *321*, 651.
[7] L. L. Zhang, X. S. Zhao, *Chem. Soc. Rev.* **2009**, *38*, 2520.
[8] V. Augustyn, P. Simon, B. Dunn, *Energy Environ. Sci.* **2014**, *7*, 1597.
[9] M. R. Lukatskaya, S. Kota, Z. Lin, M. Zhao, N. Shpigel, M. D. Levi, J. Halim, P. Taberna, M. W. Barsoum, P. Simon, Y. Gogotsi, *Nat. Energy* **2017**, *2*, 17105.
[10] B. Anasori, M. R. Lukatskaya, Y. Gogotsi, *Nat. Rev. Mater.* **2017**, *2*, 16098.
[11] M. Naguib, M. Kurtoglu, V. Presser, J. Lu, J. Niu, M. Heon, L. Hultman, Y. Gogotsi, M. W. Barsoum, *Adv. Mater.* **2011**, *23*, 4248.
[12] M. A. Hope, A. C. Forse, K. J. Griffith, M. R. Lukatskaya, M. Ghidiu, Y. Gogotsi, C. P. Grey, *Phys. Chem. Chem. Phys.* **2016**, *18*, 5099.
[13] M. Alhabeb, K. Maleski, B. Anasori, P. Lelyukh, L. Clark, S. Sin, Y. Gogotsi, *Chem. Mater.* **2017**, *29*, 7633.
[14] M. R. Lukatskaya, O. Mashtalir, C. E. Ren, Y. Dall'Agnese, P. Rozier, P. L. Taberna, M. Naguib, P. Simon, M. W. Barsoum, Y. Gogotsi, *Science* **2013**, *341*, 1502.
[15] M. Ghidiu, M. R. Lukatskaya, M. Q. Zhao, Y. Gogotsi, M. W. Barsoum, *Nature* **2014**, *516*, 78.
[16] S. Kajiyama, L. Szabova, H. Iinuma, A. Sugahara, K. Gotoh, K. Sodeyama, Y. Tateyama, M. Okubo, A. Yamada, *Adv. Energy Mater.* **2017**, *7*, 1601873.
[17] X. Wang, S. Kajiyama, H. Iinuma, E. Hosono, S. Oro, I. Moriguchi, M. Okubo, A. Yamada, *Nat. Commun.* **2015**, *6*, 6544.
[18] Y. Dall'Agnese, P. L. Taberna, Y. Gogotsi, P. Simon, *J. Phys. Chem. Lett.* **2015**, *6*, 2305.
[19] Y. Y. Peng, B. Akuzum, N. Kurra, M. Q. Zhao, M. Alhabeb, B. Anasori, E. C. Kumbur, H. N. Alshareef, M. D. Ger, Y. Gogotsi, *Energy Environ. Sci.* **2016**, *9*, 2847.
[20] N. Kurra, B. Ahmed, Y. Gogotsi, H. N. Alshareef, *Adv. Energy Mater.* **2016**, *6*, 1.
[21] J. Sun, C. Wu, X. Sun, H. Hu, C. Zhi, L. Hou, C. Yuan, *J. Mater. Chem. A* **2017**, *5*, 9443.
[22] B. E. Conway, *Electrochemical Supercapacitors: Scientific Fundamentals and Technological Applications*, Plenum Publishers, New York **1999**.
[23] F. Wang, S. Xiao, Y. Hou, C. Hu, L. Liu, Y. Wu, *RSC Adv.* **2013**, *3*, 13059.
[24] C. C. Hu, K. H. Chang, M. C. Lin, Y. T. Wu, *Nano Lett.* **2006**, *6*, 2690.
[25] T. Liu, W. G. Pell, B. E. Conway, *Electrochim. Acta* **1997**, *42*, 3541.
[26] S. Trasatti, G. Buzzanca, *J. Electroanal. Chem. Interfacial Electrochem.* **1971**, *29*, A1.
[27] W. Dmowski, T. Egami, K. E. Swider-Lyons, C. T. Love, D. R. Rolison, *J. Phys. Chem. B* **2002**, *106*, 12677.
[28] L. Y. Chen, Y. Hou, J. L. Kang, A. Hirata, T. Fujita, M. W. Chen, *Adv. Energy Mater.* **2013**, *3*, 851.
[29] B. Shen, X. Zhang, R. Guo, J. Lang, J. Chen, X. Yan, *J. Mater. Chem. A* **2016**, *4*, 8180.
[30] J. Zhang, J. Jiang, H. Li, X. S. Zhao, *Energy Environ. Sci.* **2011**, *4*, 4009.
[31] B. G. Choi, S. J. Chang, H. W. Kang, C. P. Park, H. J. Kim, W. H. Hong, S. Lee, Y. S. Huh, *Nanoscale* **2012**, *4*, 4983.
[32] A. D. Dillon, M. J. Ghidiu, A. L. Krick, J. Griggs, S. J. May, Y. Gogotsi, M. W. Barsoum, A. T. Fafarman, *Adv. Funct. Mater.* **2016**, *26*, 4162.
[33] K. Hantanasirisakul, M. Q. Zhao, P. Urbankowski, J. Halim, B. Anasori, S. Kota, C. E. Ren, M. W. Barsoum, Y. Gogotsi, *Adv. Electron. Mater.* **2016**, *2*, 1.
[34] K.-H. Chang, C.-C. Hu, *Electrochem. Solid-State Lett.* **2004**, *7*, A466.
[35] T. Hu, J. Wang, H. Zhang, Z. Li, M. Hu, X. Wang, *Phys. Chem. Chem. Phys.* **2015**, *17*, 9997.
[36] J. Ryan, A. Berry, M. Anderson, J. Long, R. Stroud, V. Cepak, V. Browning, D. Rolison, C. Merzbacher, *Nature* **2000**, *406*, 169.
[37] M. R. Lukatskaya, S. M. Bak, X. Yu, X. Q. Yang, M. W. Barsoum, Y. Gogotsi, *Adv. Energy Mater.* **2015**, *5*, 1500589.
[38] J. Wang, J. Polleux, J. Lim, B. Dunn, *J. Phys. Chem. C* **2007**, *111*, 14925.
[39] M. Toupin, T. Brousse, D. Bélanger, *Chem. Mater.* **2004**, *16*, 3184.
[40] Z. Dai, C. Peng, J. H. Chae, K. C. Ng, G. Z. Chen, *Sci. Rep.* **2015**, *5*, 9854.

[41] Z. S. Wu, W. Ren, D. W. Wang, F. Li, B. Liu, H. M. Cheng, *ACS Nano* **2010**, *4*, 5835.

[42] Z. S. Wu, D. W. Wang, W. Ren, J. Zhao, G. Zhou, F. Li, H. M. Cheng, *Adv. Funct. Mater.* **2010**, *20*, 3595.

[43] S. Chan Lee, U. M. Patil, S. J. Kim, S. Ahn, S.-W. Kang, S. C. Jun, *RSC Adv.* **2016**, *6*, 43844.

[44] C. Zhang, J. Xiao, L. Qian, S. Yuan, S. Wang, P. Lei, *J. Mater. Chem. A* **2016**, *4*, 9502.

[45] W. Liu, X. Yan, J. Chen, Y. Feng, Q. Xue, *Nanoscale* **2013**, *5*, 6053.

[46] P. Huang, C. Lethien, S. Pinaud, K. Brousse, R. Laloo, V. Turq, M. Respaud, A. Demortiere, B. Daffos, P. L. Taberna, B. Chaudret, Y. Gogotsi, P. Simon, *Science* **2016**, *351*, 691.

[47] M. F. El-Kady, R. B. Kaner, *Nat. Commun.* **2013**, *4*, 1475.

[48] M. Beidaghi, C. Wang, *Adv. Funct. Mater.* **2012**, *22*, 4501.

[49] J. Lin, C. Zhang, Z. Yan, Y. Zhu, Z. Peng, R. H. Hauge, D. Natelson, J. M. Tour, *Nano Lett.* **2013**, *13*, 72.

[50] Q. Jiang, N. Kurra, C. Xia, H. N. Alshareef, *Adv. Energy Mater.* **2017**, *7*, 1601257.